Volume 1 | Number 1 | Jan 2013 | Pages 1–100

PCCP

Physical Chemistry Chemical Physics
www.rsc.org/pccp

ROYAL SOCIETY
OF CHEMISTRY

ROYAL SOCIETY
OF CHEMISTRY

www.rsc.org/pccp

Journal Name

ARTICLE

Electrodeposition of FeCrNi stainless steel: Microstructural changes induced by anode reactions

Madoka Hasegawa[a*], Songhak Yoon[b], Gaylord Guillonneau[a], Yucheng Zhang[a,b], Cédric Frantz[a], Christoph Niederberger[a,d], Anke Weidenkaff[b,e], Johann Michler[a,d], and Laetitia Philippe[a,d]

The FeCrNi alloy, whose composition is close to that of stainless steel 304, was prepared by electrodeposition and characterized. Nanocrystalline FeCrNi (nc-FeCrNi) was obtained by employing a double-compartment cell where the anode is separated from the cathode compartment, while amorphous FeCrNi (a-FeCrNi) was deposited in a conventional single electrochemical cell. The carbon content of nc-FeCrNi was found to be significantly lower than that of a-FeCrNi, suggesting that carbon inclusion is responsible for the change in microstructure. The major source of carbon is associated with the reaction compounds at the anode electrode, presumably decomposed glycine. Crystal structure analysis with XRD and TEM revealed that the as-deposited nc-FeCrNi deposits consist of α-Fe which transforms to γ-Fe upon thermal annealing. Nanoindentation tests showed that nc-FeCrNi exhibits higher hardness than that of a-FeCrNi, which is consistent with the inverse Hall-Petch behavior.

Introduction

The microstructure of materials significantly influences mechanical and physical properties in many ways. Especially the grain size is of prime importance because it is a dominant factor which determines the mechanical properties of materials. As described by the well-known Hall-Petch relationship, the yield strength and hardness increases with a decrease of grain size down to some tens of nanometers range,[1, 2] where the blocking of dislocation diffusion by the grain boundary strongly influences the mechanical deformation. Therefore, nanocrystalline metals exhibit outstanding properties. Nanocrystalline metals have been synthesized by various techniques including ball milling,[3] consolidation,[4] condensation[5] and electrodeposition.[6] Synthesis of nanocrystalline stainless steel, which is a very important material due to its excellent corrosion resistance, has also been investigated, aiming at further improvement of its mechanical properties. The synthesis techniques employed for nanocrystalline stainless so far include bulk nanocrystalline synthesis by *in-situ* consolidation,[7] grain refinement of cold-rolled foil via phase transformation cycling during gaseous nitriding,[8] surface nanocrystallization by sand blasting,[9] surface mechanical attrition[10-13] and ultrasonic shot peening.[14] It has been reported that the hardness and the yield strength of such nanocrystalline stainless steels are superior to those of the coarse-grained stainless steel.[9, 10, 13] Moreover, the surface-nanocrystallization-treated stainless steel exhibits an excellent corrosion resistance even better than the conventional coarse-grained stainless steel.[9]

Electrodeposition is one of the most promising techniques to synthesize metal films with a controlled microstructure. Electrodeposition of such functional alloys is significant because it is a unique technique to fill high aspect-ratio structures used in the LIGA [a German acronym for Lithographie, Galvanoformung, Abformung (Lithography, Electroplating, and Molding)] process,[15] which is a key process technology for fabricating high-precision microcomponents with controlled properties. Electrodeposition of Fe-based alloys with the composition similar to that of stainless steels have been investigated for many years and various electroplating baths have been proposed so far, as reviewed previously.[16] However, in spite of numerous efforts, the technique has not been established for the practical applications due to the complexity of the bath electrochemistry. In addition to the anomalous codeposition known for the Fe-Ni plating system,[17] the instability of trivalent Cr ions in the bath is the major challenge for FeCrNi electrodeposition. The aqua-chromium complex $Cr(H_2O)_6^{3+}$ is not themodynamically stable in water

and therefore tends to experience olation which results in formation of the hydrolyzed polymers. In acidic aqueous baths, the reduction of trivalent chromium ions occurs in two steps:[18]

$Cr^{3+} + e^- \rightarrow Cr^{2+}$ (E^0 = -0.407 V vs. NHE)

$Cr^{2+} + 2e^- \rightarrow Cr$ (E^0 = -0.913 V vs. NHE)
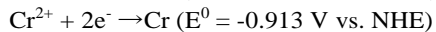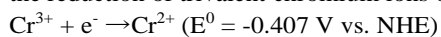
Hence, the deposition of Cr is accompanied by hydrogen evolution from oxidation of proton and water:

$2H+ + 2e^- \rightarrow H_2\uparrow$ (E^0 = +0.000 V vs. NHE)

$H_2O + 2e^- \rightarrow H_2\uparrow + 2OH^-$ (E^0 = -0.828 V vs. NHE)
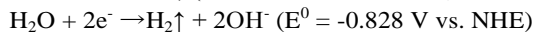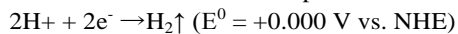
The significant hydrogen evolution brings about not only a decrease in the current efficiency but also an increase in the local pH adjacent to the cathode surface, leading to the formation of hydrolyzed chromium polymers which inhibit the cathode reactions. Thus, in order to prevent chromium ions from forming the hydrolyzed polymers, the use of a complexing agent is inevitable for the Cr and Cr-alloy electrodeposition. Philippe and co-workers[19] have investigated various complexing agents for the FeNiCr alloy electrodeposition and found that glycine is a suitable complexing agent of trivalent Cr ions for achieving reproducible and stable composition. Recently, further studies have been conducted based on this electroplating bath and we have demonstrated that FeCrNi electrodeposits with a composition similar to that of stainless steel 304 (18%Cr and 8%Ni) can be deposited in 300-µm-deep UV-LIGA molds[20], although some issues such as the surface cracking and the residual stress deformation remained to be addressed. In order to overcome these challenges, further studies on the microstructure of FeCrNi electrodeposits as well as electrochemistry of the plating bath are essential. In the FeCrNi electroplating bath, several side reactions are expected in addition to the cathodic reduction of Fe-Cr-Ni alloy. These reactions include the anodic oxidation reactions of bath constituents which may modify the reactions at the cathode. In order to identify the impacts of anode reactions on the FeCrNi deposition, we conducted the electrodeposition studies in the double compartment cell system where the anode electrode is separated from the cathode electrode compartment, and discussed the effects of the anodic reaction on the microstructure of the FeCrNi electrodeposits. Furthermore, the effects of the microstructure on mechanical properties of FeCrNi deposits were investigated.

Experimental Methods

Electrodeposition of FeCrNi was performed employing two types of electrochemical cells: a conventional single-compartment cell (single-cell) and a double-compartment cell (double-cell), as shown in Fig. 1. The double-cell consists of the cathode and anode compartments which are connected through a saturated KCl salt bridge gelatinized with agar. The cathode compartment was filled with the electroplating bath, while the anode compartment was filled with saturated KCl aqueous solution. Both electrochemical cells are equipped with a water jacket for temperature control of electroplating bath. The temperature of the electroplating bath was controlled at 22°C with an error of +/- 0.5°C by employing a temperature controlled circulator (Julabo, F12-ED). FeCrNi alloy was electrodeposited on a Si substrate covered with a sputter coated Au layer (100 nm) on a Cr adhesion layer (5 nm). Prior to electrodeposition experiments, the substrate was cleaned in freshly prepared Piranha solution (30% H_2O_2 : H_2SO_4= 1 : 3) for at least 10 min and thoroughly rinsed in deionized water (18.2 MΩcm). Subsequently, the conductive surface of the substrate was covered with a masking tape leaving a deposition area (1.5 cm × 1.5 cm). A saturated calomel electrode (SCE) was used as the reference electrode to monitor the potential of electrodeposition. A Pt plated Ti mesh was used as the counter electrode. Electrodeposition of FeCrNi was performed galvanostatically at -100mA/cm^2 using a potentiostat (PGSTAT 30, Autolab) controlled either by GPES or NOVA (version 1.7) software.
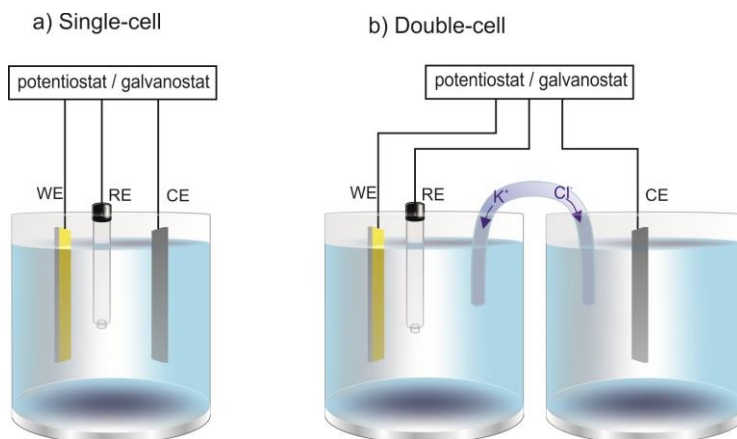

Fig. 1. Electrochemical cells for FeCrNi electrodeposition: (a) single-cell and (b) double-cell.

The bath composition of FeCrNi electrodeposition is shown in Table 1. All the chemicals were of reagent grade (Sigma-Aldrich) and were used as-received without any further purification. For the bath preparation, firstly, chromium chloride and glycine were added to deionized water in a glass beaker and thoroughly mixed. The electrolyte was heated at 80ºC at least for 30 min in order to complete the complexing reaction of Cr ions and glycine. Afterward, the bath was cooled down to room temperature and kept overnight. In a separate beaker, the rest of bath components were mixed. Subsequently, the solution was added to the Cr-glycine solution at room temperature. Finally, the solution pH along with the bath volume was adjusted.

Table 1. Bath composition for FeCrNi electrodeposition

	concentration (mol/L)
$CrCl_3 \cdot 6H_2O$	0.4
glycine (H_2NCH_2COOH)	0.4
$FeCl_2 \cdot 4H_2O$	0.03
$NiCl_2 \cdot 6H_2O$	0.2
NH_4Cl	0.5
H_3BO_3	0.15
NaCl	0.5

*pH: 1 (adjusted with HCl or NH_4OH)

**Temperature: 22ºC

Deposit morphology was observed by field-emission scanning electron microscopy (FE-SEM, Hitachi S4800). Crystal structures of FeCrNi electrodeposits and their evolution under thermal annealing were characterized by *in-situ* grazing-incidence X-ray diffraction (GI-XRD). GI-XRD was carried out using a PANalytical X'Pert PRO MPD θ-θ scan system equipped with an X-ray mirror and a parallel plate collimator. The incident X-rays had a wavelength of 1.5418 Å (Cu-Kα radiation) and the incident angle was fixed to 10°. The diffraction patterns were scanned 20 to 90° (2θ) with an angular step interval of 0.05°. The samples were placed in the heating chamber (XRK 900, Anton Paar) and were heated under 5% H_2 (99.999%, Messer) in N_2 (99.999%, Messer) using a flow rate of 100 mL/min in the temperature range 30 to 800 °C with a heating rate of 40 K/min. Further analysis of the microstructure of FeCrNi electrodeposits was performed by transmission electron microscope (TEM, JEOL 2200 FS). TEM lamellae of the samples were prepared by FIB-milling (VELA FIB/SEM, TESCAN). TEM analysis was carried out with an acceleration voltage of 200 kV using techniques including selected area diffraction (SAD), bright field (BF), dark field (DF) and high-resolution imaging. For both BF and DF imaging, an objective lens aperture (OLA) of 20 μm diameter has been used. The dark field images were obtained by selecting a random part of the diffraction ring with the OLA.

The chemical compositions of FeCrNi deposits were measured by glow discharge optical emission spectroscopy (GDOES, JY 5000 RF, HORIBA Jobin Yvon). The concentrations of Fe, Cr, Ni and C were measured for all FeCrNi samples. In addition to these elements, the measurements showed that the films also contain a certain amount of oxygen. The oxygen concentration was measured to be approximately 2 wt% in average for the deposits obtained with both growth conditions, although this concentration level is under the lower limit of reliable oxygen measurements for the GDOES machine used in this study. Deposit thickness was estimated from the GDOES depth profiles. For some selected samples, thickness measurements were performed also by SEM observations of sample cross-sections. We confirmed that thickness values from both methods are similar to each other.

The anode reactions in the FeCrNi electroplating bath were analyzed by cyclic voltammetry. A Pt disk electrode embedded in PEEK with a diameter of 1.5 mm was employed as the working electrode. Pt wire was used as the counter electrode, while a SCE was used as the reference electrode. Prior to each measurement, the Pt working electrode was mechanically polished with alumina paste, and then rinsed in deionized water followed by cleaning in acetone and ethanol with sonication. Subsequently, the electrochemical cleaning of electrode was performed at the constant potential +1.0 V for 2 min in 0.5 M H_2SO_4 aqueous solution. Then, the electrode potential was cycled between -0.2 V and 1.2 V at 100 mV/s for 15 min. The measurements were carried out immediately after the cleaning process. The test solution was deaerated by Ar bubbling for at least 15 min prior to each measurement. Cyclic voltammetry was performed at a scan rate of 50 mV/s for 5 cycles. Only the second scan is shown in this paper because the voltammogram recorded in each cycle is essentially identical except for the first cycle for all experiments.

The Young's modulus and the hardness of the samples were measured with a Nanoindenter XP® (Agilent Technologies). A Berkovich indenter was used in the experiments. Tip area function calibration was performed on fused silica using the Oliver and Pharr method before the experiment in order to take into account the non-perfect geometry of the indenter.[21] During the loading and the unloading, a constant strain rate was applied with P'/P=0.1 s^{-1},[22] P being the applied load and P' the loading rate. The maximum displacement was 1 μm, which represents approximately 7% of the film thickness. At the maximum displacement, the load is kept constant during 15 s in order to minimize the creep and to correctly measure the stiffness during unloading. The thermal drift was corrected at the unloading by keeping a constant load during 60 s at 1% of the maximum load.[23] On each sample, 100 indents were performed. The Young's modulus and the hardness were calculated using the Oliver and Pharr method.[21]

Results

Surface morphology. The appearance of deposits obtained in the double-cell is significantly different from those deposited in the single-cell. Semi-bright deposits were obtained in the single-cell, whereas grey and dull deposits were deposited in

the double-cells. Microscopic observation further revealed a significant difference in the surface morphology of these deposits (Fig. 2). As seen in Fig. 2a, the surface of the film obtained from the single-cell is essentially very smooth without any visible surface feature, except for the portions of irregular deposits (marked by arrows). Unlike the deposit from the single-cell, large and small surface features were observed on the deposit prepared in the double-cell, suggesting growth of larger grains. We did not observe any precipitation-like deposits on this sample. As can be seen in SEM images, both samples from the single-cell and the double-cell contain cracks. Cracks were observed when the film is thicker than 5 μm. The cracking of Cr and Cr-alloy electrodeposits is believed to be related to the incorporation of the chromium hydrides (CrH and/or CrH$_2$).[24] The hydrides are unstable and therefore decompose with shrinkage in volume to metallic Cr and hydrogen atoms. We consider that cracking of the FeCrNi electrodeposits is also caused by a similar mechanism.
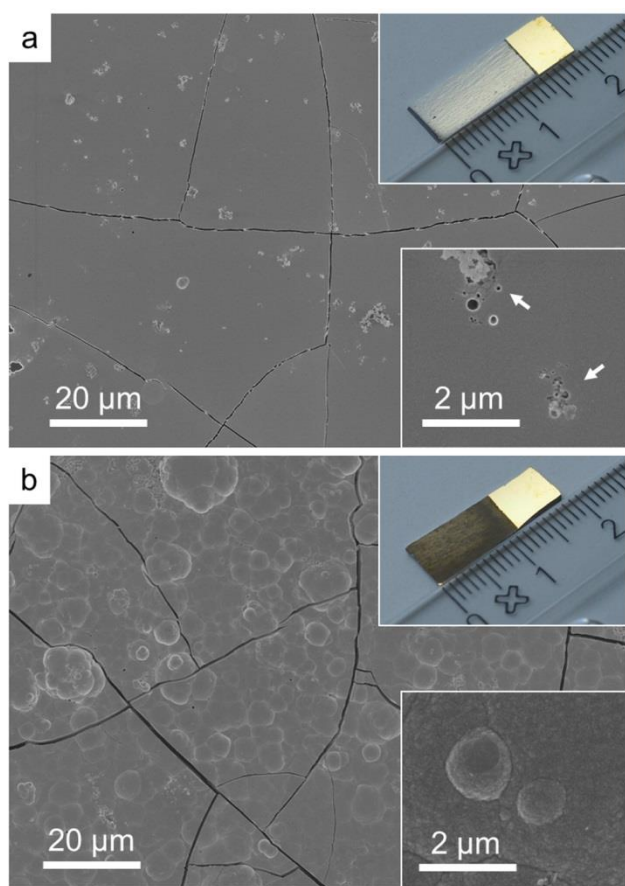

Fig. 2. Surface morphology of FeCrNi electrodeposits from (a) single-cell and (b) double-cell. Thickness of deposit is 15.7 μm for the single-cell and 14.4 μm for the double-cell, respectively.

Crystal structure. Fig. 3 shows the results of the in-situ GI-XRD measurements of a deposit prepared in the single-cell during thermal treatment up to 800°C. At 30°C, no reflections are visible in XRD pattern, suggesting that the FeCrNi film prepared in the single-cell is essentially amorphous in the as-deposited state. The amorphous phase was stable up to 300°C. Heating to 400°C, a broad peak at 45°, which is identified as the (111) reflection of α-Fe, started to appear, showing the onset of crystallization. From 550°C, new peaks are visible at around 43°, 50°, 74° and 90°, which are identified as the reflections of γ-Fe. At 600°C, the peaks of γ-Fe increased while the peak at 45° of α-Fe completely disappeared, demonstrating the phase transformation from α-Fe to γ-Fe. Above 600°C, several small peaks are visible and they became distinctive at higher temperatures. These peaks are indexed to the iron oxides such as Fe$_3$O$_4$ and α-Fe$_2$O$_3$.[25]

The same GI-XRD experiments were performed for a deposit obtained in the double-cell (Fig. 4). For this sample, a peak at 45° of α-Fe was clearly observed at 30°C, showing that the deposit is already crystalline in the as-deposited state. The α phase transformed to γ-Fe at 500°C, which is 50°C lower compared to a similar deposit prepared from the single-cell. The iron oxide peaks also appear from above 600°C. It is worth noting that the electrodeposited nc-FeCrNi was found to consist of α-Fe in contrast to the thermally prepared FeCrNi alloys with a similar Fe-Cr-Ni composition, which consist of γ-Fe. The formation of such a metastable phase is quite common in films obtained by electrodeposition which is a non-equilibrium deposition technique. Most of electrodeposited FeCrNi alloys reported so far are amorphous[26-28] or ultrafine-grained nanocrystalline,[29-31] although the microstructure is not investigated in details for many cases. The formation of the α phase is reported in a similar chloride-based FeCrNi electroplating baths,[29] while γ-Fe formation is observed in an aqueous chloride-sulfate based bath[31] and a non-aqueous bath.[32] Hence, it seems that the chemistry of the bath significantly influences the microstructure. The in-situ GI-XRD also showed that a-FeCrNi electrodeposits firstly recrystallized to form the α phase before it transforming into the γ phase. This indicates that a-FeCrNi in the as-deposited state possesses a local crystal structure similar to that of nc-FeCrNi in short range order, although a-FeCrNi is more disordered. It should also be pointed out that we observed evidence of formation of iron oxides during thermal treatment in deposits obtained from both setups. Because the heat treatment is performed in a slightly reducing atmosphere, this result suggests that the FeCrNi samples contain non-negligible amounts of oxygen in the as-deposited state, although we were not able to precisely quantify the oxygen content with the available equipment.
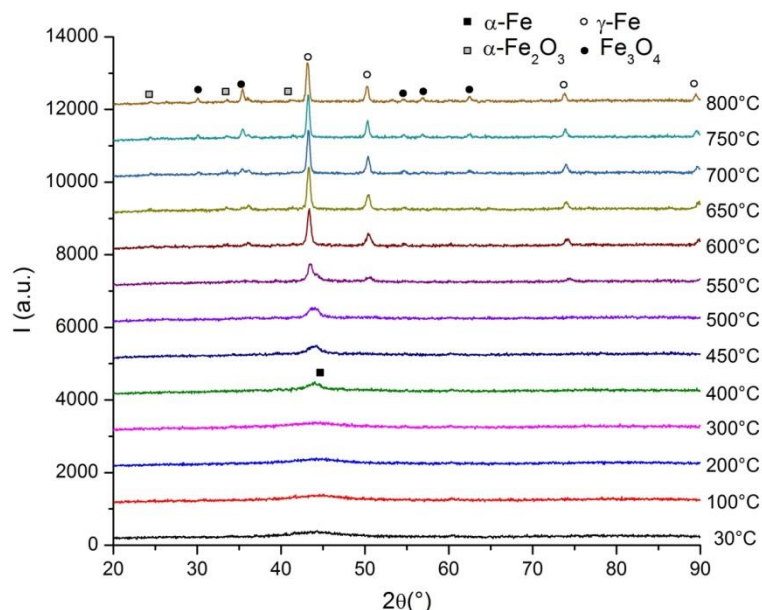
Fig. 3. GI-XRD measurements of a FeCrNi electrodeposit obtained in the single-cell.
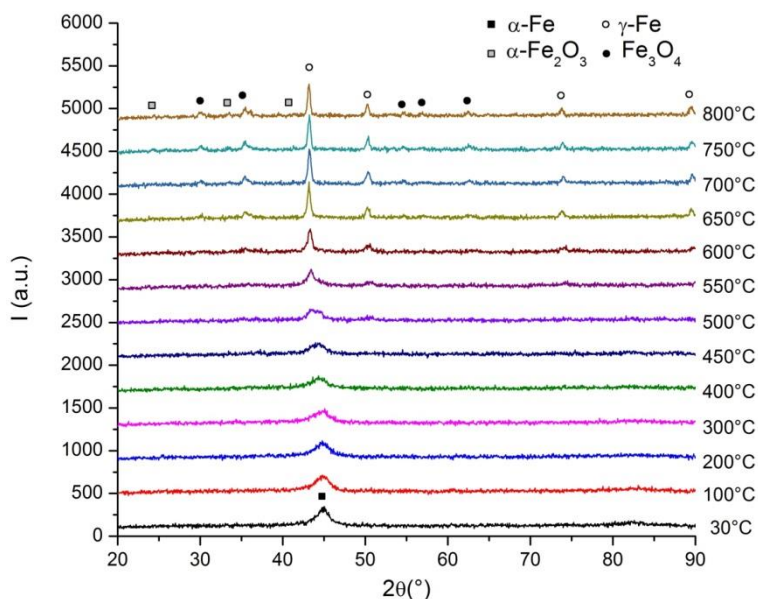

Fig. 4. GI-XRD measurements of a FeCrNi electrodeposit obtained in the double-cell.

The microstructure of FeCrNi deposits was further investigated by TEM. Fig. 5 shows the TEM images and the electron diffraction (ED) pattern of an as-deposited FeCrNi film from the single-cell. The typical halo pattern in the ED clearly shows that the deposit is amorphous.

On the other hand, nanocrystalline grains were observed in the deposit from the double-cell (Fig. 6a,b). The rings in the ED (Fig. 6c) reveal that the deposit is polycrystalline with no preferred orientation. From the diffraction rings, we observe only α-Fe phase, which is fully consistent with the results of XRD described previously. The dark field image (Fig. 6d) taken at a selected area of the ED (indicated with a white circle) shows the existence of nanometer grains. Although there are some relatively larger grains near the edge of sample (marked with an arrow), we confirmed that they are an artifact caused by FIB-milling and/or exposure to the electron beam for TEM observation. Thus the grain size of the as-deposited film is considered to be less 10 nm. Furthermore, observation of BF images while the sample was tilted showed that the presence of amorphous regions among the nanocrystalline grains,

suggesting that the film consists of nanocrystalline grains dispersed in an amorphous matrix.
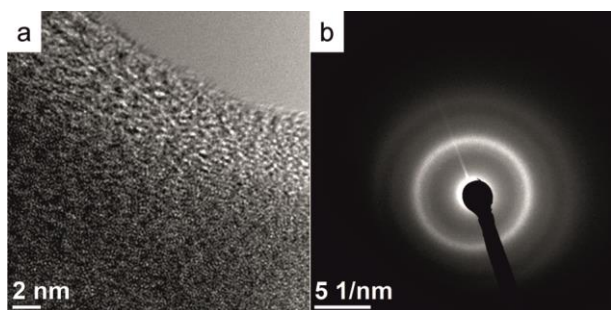

Fig. 5. TEM micrograph of a FeCrNi electrodeposit from the single-cell: (a) high-resolution image, and (b) electron diffraction pattern.
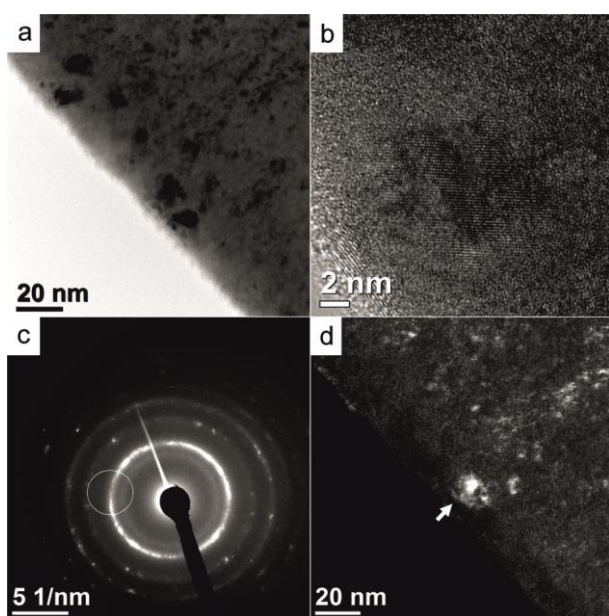

Fig. 6. TEM micrograph of a FeCrNi electrodeposit from the double-cell: (a) bright field image, (b) high-resolution image, (c) electron diffraction pattern and (d) dark field image. The white circle in diffraction pattern represents the aperture used to record the dark field image.

Chemical composition. The chemical compositions of FeCrNi deposits were measured by GDOES. For this experiment, a series of electrodeposition was performed in a plating bath and the composition change with respect to the aging of the bath was examined.

Fig. 7 compares the chemical compositions of FeCrNi electrodeposits from the single-cell and the double-cell. We defined the aging factor (C/L) as the total electron charge which has been applied to the system before starting a specific

deposition divided by the bath volume. For both cell setups, the concentrations of Fe, Cr and Ni are similar each other and stable until 3000-4000 C/L, where the composition starts to change due to the depletion of ferrous ions.
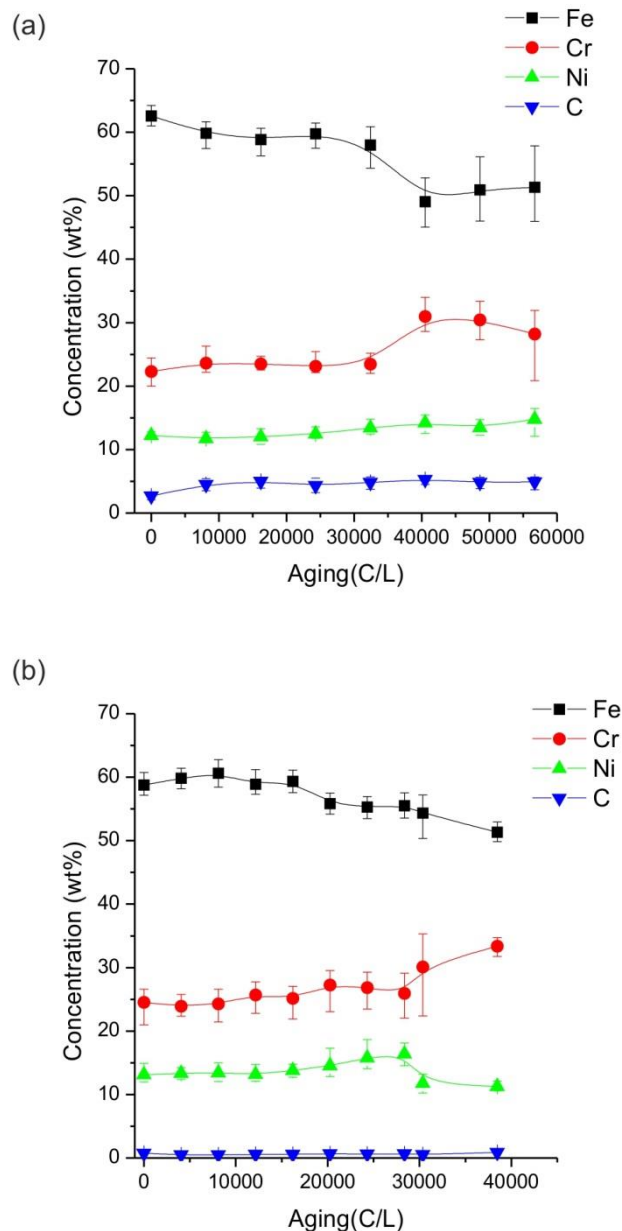
Fig. 7. The composition of FeCrNi electrodeposits from (a) single-cell and (b) double-cell.

In contrast, a significant difference between the single and double-cells was found in the carbon concentration. The carbon concentration in the deposits produced in the double-cell was 0.6 wt% in average whereas the carbon concentration of the deposits from the single-cell is approximately 5 wt%. The experiments also revealed that, in the case of the single-cell,

carbon concentration continuously increased at the initial stage up to 16000 C/L, where the concentration reaches the saturation value (5 wt%). Afterwards, the concentration became constant over time. It should be also noted that this saturated value was maintained even after the concentration of Fe, Cr and Ni started to change by aging (30000-40000 C/L), suggesting that the major source of carbon is not related to the reduction of the chromium(III)-glycine complex. On the other hand, carbon concentration in the case of the double-cell was remained almost constant at 0.6 wt% throughout the experiment. Accordingly, the carbon inclusion is attributed to the anode reaction product which subsequently affects the reaction at the cathode. It is also considered that this difference in carbon concentration causes the difference in microstructure of the deposits obtained from the single-cell and the double-cell. The high carbon concentration in the deposits from the single-cell is thought to be responsible for the amorphous phase formation, whilst the low carbon concentration in the deposits from the double-cell is considered to stimulate the crystallization of the films, leading to the nc-FeCrNi formation.

Deposition rate. The deposition rate is correlated to the carbon concentration in a resulting deposit. Fig. 8 displays the deposition rate with respect to the aging of electrolyte in different growth conditions. The deposition rate in the single-cell was initially 15.7μm/h and it drastically decreased to a less than half value during first 16000 C/L, which corresponds to the period in which the carbon concentration increased with aging of the electrolyte (Fig. 7a). Assuming that the density of deposits is similar to that of 304 stainless steel, the current efficiency is calculated to be 14% in a non-used bath and around 5% in an aged bath (40000 C/L), respectively. Unlike the case of the single-cell, such remarkable changes in the deposition rate were not observed in the case of the double-cell. Instead, we observed a trend that the deposition rate gradually decreases with an increase in the aging factor.
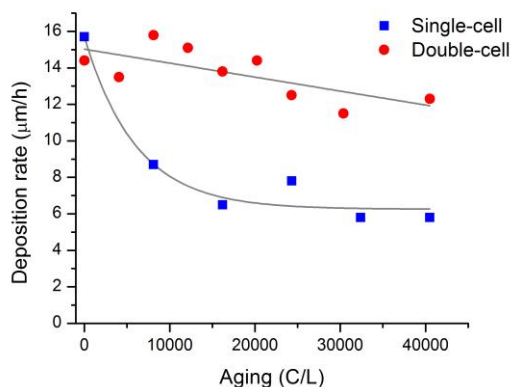

Fig. 8. Deposition rate in single cell (blue square) and double-cell (red circle).

Anode reactions in the FeCrNi plating bath. In order to obtain insights into the enhanced carbon inclusion for the deposits from the single-cell, the anode reactions in the FeCrNi plating bath were investigated by a series of cyclic voltammetry experiments. For simplicity, the measurements were carried out on a Pt disk electrode instead of a Pt-coated Ti mesh electrode employed for the FeCrNi electrodeposition experiments. We especially focused our attention on the reactions of glycine, which is the only organic compound in the bath. Fig. 9a shows the cyclic voltammograms of glycine in a simple acid solution. The addition of glycine and an increase in its concentration results in an increase of the anode current at around +1.1 V, which overlaps with the current wave for Pt oxidation. In addition, the presence of glycine brings about the cathode shift of the peak for platinum oxide reduction at -0.5 V as well as the peaks for the adsorption/deposition of hydrogen, suggesting the interaction of glycine with the cathode as reported previously.[33] Because the height of the reduction wave of Pt oxide does not increase while the anode wave from +0.5 V to +1.2 V increases, the increase in the anodic current is attributed to the anodic reaction of glycine rather than the enhanced Pt oxide formation. Voltammetric studies were performed in the chloride-based acid solution, which is more similar to the FeCrNi plating bath. Fig. 9b shows the cyclic voltammograms in 0.4 M NaCl aqueous solution without (i) and with (ii) 0.4 M of glycine. An aqueous solution of HCl was added to adjust the solution pH to 1, which is the same value as that of the FeCrNi plating bath. Similar to the result in a H_2SO_4 solution, an increase of the anode current was observed at +0.5 to +1.0 V by the addition of glycine (inset), although the effect was more difficult to observe due to the chlorine evolution which starts at around +1.0 V. A more extended potential sweep revealed that the anodic wave from +1.2 to +1.7 V in the glycine-containing solution is significantly larger than that in the NaCl solution without glycine, demonstrating the anodic reaction of glycine at these potentials. It should be noted here that the potential of the anode electrode during FeCrNi electrodeposition in the single-cell was from +1.5 to +1.7V vs. SCE. Therefore we suspect that the oxidation product of glycine which is accumulated in the bath with time is related to the carbon inclusion.

In order to obtain further insights into the anodic reactions in the FeCrNi electroplating bath, cyclic voltammetry was performed in the solutions containing various combinations of the bath constituents: the whole FeCrNi plating bath (FeCrNi bath), a bath without ferrous and trivalent chromium ions (Cr bath), a bath without containing any metal ions (Glycine bath) and a base electrolyte which contains neither metal ions nor glycine (Base electrolyte), as shown in Table 2. Fig. 10a displays the cyclic voltammogram of Pt in the FeCrNi bath. Reversible oxidation-reduction peaks (+0.5V vs. SCE) correspond to those of a ferrous-ferric reaction. An increase in the anode current at +1.0 V is due to the chlorine evolution by oxidation of chloride ions. Due to the large anodic current of ferrous ions, the effect of glycine was not able to be observed in this bath. A further potential sweep to more anodic potentials was performed in the same bath (Fig. 10b). The voltammogram

revealed a large anodic wave from +1.2 to +1.5 V. Such a large anodic peak was also observed in the voltammograms in the other baths (Fig. 10c-e). Because the anodic wave in the base electrolyte (Fig. 10e) is much larger than that observed in a NaCl solution (Fig. 9b), several anodic reactions seem to occur in addition to the chlorine evolution. We also found that the anodic wave is larger in the FeCrNi and Cr baths than in the other solutions (the Glycine bath and the base electrolyte). This implies that the anodic wave is also associated with the oxidation of trivalent Cr ions to hexavalent ions along with the chlorine evolution. Apart from the anodic peaks discussed above, there are two cathodic waves at +0.8 V and +0.4 V,

respectively. The former wave might be due to the reduction of chlorine absorbed on the electrode. Although they are not fully identified, the latter wave may correspond to the reduction wave of hexavalent chromium ions to trivalent ions, according to Welch and co-workers,[34] who observed its reduction peak from +0.25 to +0.27 V vs. SCE on various electrodes. In addition to the oxidation of chromium ions, the reduction of Pt oxide should occur in this potential region, which may explain the small cathodic wave observed at +0.4 to +0.5 V in the solutions which contain neither Fe nor Cr ions (curves d and e in Fig. 10).
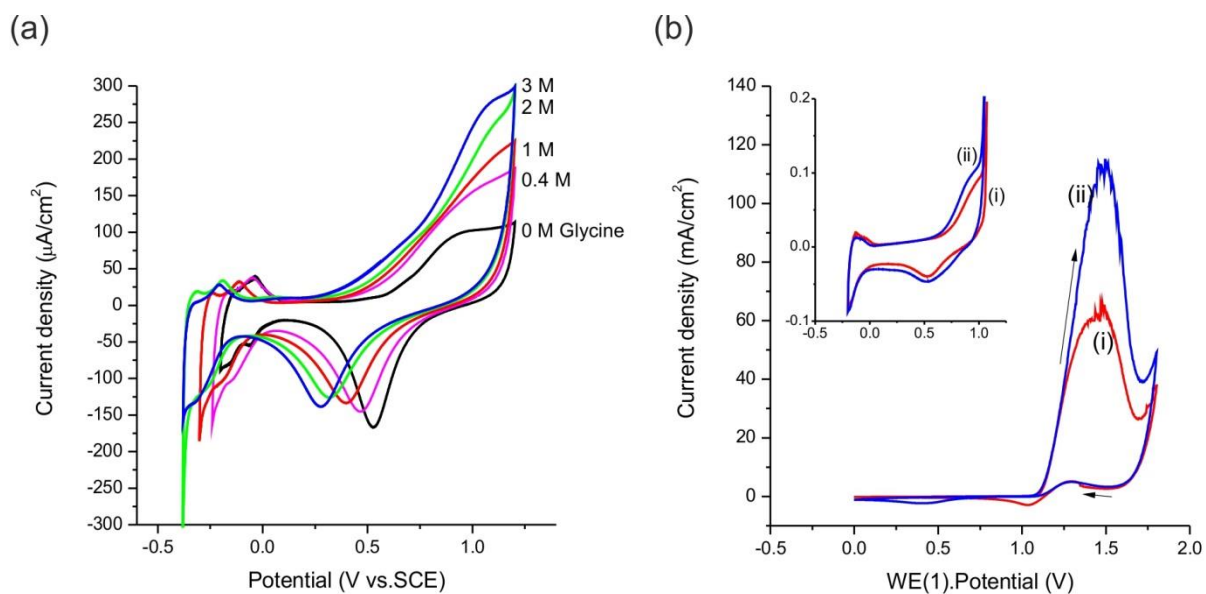

Fig. 9. Cyclic voltammetry of glycine on a Pt disk electrode (ø1.5 mm): (a) various concentrations of glycine with 0.5 M H₂SO₄, and (b) 0.5 M NaCl aqueous solution (pH 1, adjusted with HCl) (i) without and (ii) with 0.4 M glycine.

Table 2. Composition of the eletrolytes for cyclic voltammerty

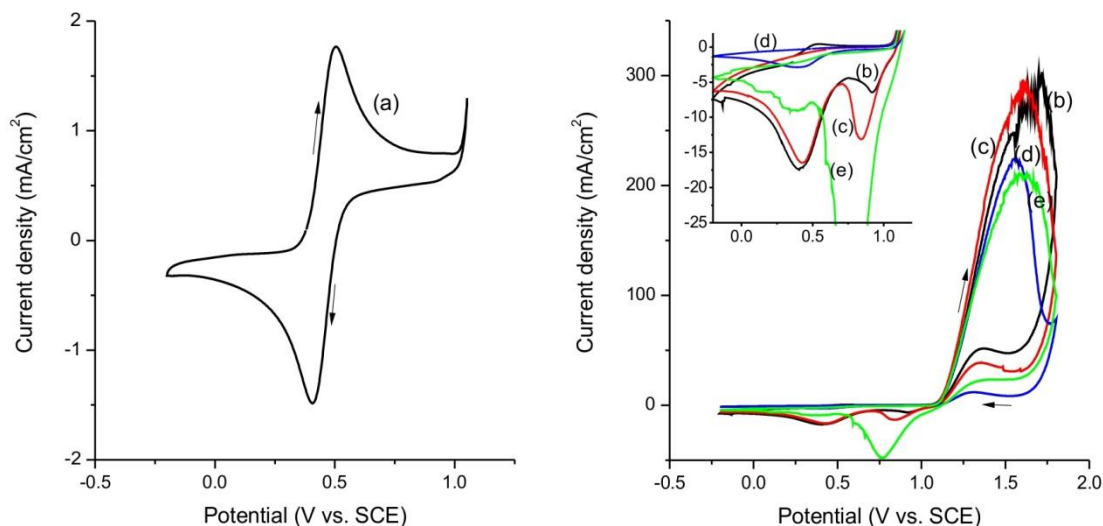|	Concentration (mol/L)			
	FeCrNi bath	Cr bath	Glycine bath	Base electrolyte
CrCl₃·6H₂O	0.4	0.4	-	-
FeCl₂·4H₂O	0.03	-	-	-
NiCl₂·6H₂O	0.2	-	-	-
Glycine	0.4	0.4	0.4	-
NH₄Cl	0.5	0.5	0.5	0.5
H₃BO₃	0.15	0.15	0.15	0.15
NaCl	0.5	0.5	0.5	0.5

Fig. 10. Cyclic voltammetry on a Pt disk electrode (ø1.5 mm) in (a and b) FeCrNi bath, (c) Cr bath, (d) Glycine bath and (e) Base electrolyte.

Mechanical properties. The mechanical properties of FeCrNi deposits were investigated by nanoindentation tests. Table 3 lists the results of the indentation tests of the deposits from the single- and double-cells. The hardness is higher for deposits from the double-cell (nc-FeCrNi) than that from the single-cell (a-FeCrNi). The results can be explained by the inverse Hall-Petch behavior, in which the breakdown of the classical Hall-Petch relation occurs in nanocrystalline materials with a grain size of typically 10 nm and smaller,[35, 36] even down to amorphous materials.[37, 38] In contrast to the classical Hall-Petch relationship, the hardness values of such materials have been shown to decrease with a decrease in the grain size. The Young's modulus obtained for the two growth conditions is very similar (4% difference), the value for the single cell (a-FeCrNi) being smaller than the value obtained for the double-cell (nc-FeCrNi). This difference is consistent with literature results showing a decrease of the Young's modulus with the grain size for nanocrystalline metals and alloys[23, 36] for grain sizes smaller than 20nm. These modulus values are low in comparison to those of conventional stainless steels. This is attributed to the presence of an amorphous phase which has a larger free volume fraction than that for a crystalline phase, causing a softening of the material.[39-42]

Table 3. Mechanical properties of FeCrNi deposits from the single cell (a-FeCrNi) and the double cell (nc-FeCrNi).

	Single-cell	Double-cell
Young's modulus (GPa)	142.63	148.45
St. dev. (GPa)	17.80	39.91
Hardness (GPa)	4.07	4.8
St. dev. (GPa)	0.51	1.12

Discussion

FeCrNi electrodeposits grown in the double-cell are found to be nanocrystalline, whereas those obtained for the single-cell are amorphous. The change in microstructure is attributed to the difference in carbon concentration. The typical carbon concentration in a single-cell a-FeCrNi deposit was measured to be 5 wt%, which is much higher than the maximum solubility of carbon in steel (~2 wt% for austenitic steel). According to thermodynamic equilibrium, such a large excess of carbon inclusion should result in formation of metal carbides such as Fe$_3$C. However, the reflections of the metal carbides were not found in XRD profile of the as-deposited a-FeCrNi film. Therefore, the film should be in a supersaturated state, with the interstitial carbon atoms, thus leading to formation of amorphous phase. In contrast, a double–cell nc-FeCrNi deposit contains much less carbon. The low carbon concentration is thought to stimulate the formation of grains, resulting in the formation of nanocrystalline films.

Cyclic voltammetry studies revealed that the oxidation of glycine as well as Fe(II) and Cr(III) ions occurs at the anode. The oxidation of α-amino acids (for example, glycine, alanine,

and serine) on Pt has been known for many years.[33, 43-46] Studies have shown that these amino acids are decomposed through the Kolbe reaction followed by hydrolysis to form aldehydes during the first step of oxidation. Ammonium is formed along with carbon dioxide during this step, and accordingly, the oxidation reaction of glycine in acidic media is considered as follows:

$$CH_2(NH_3^+)COOH + H_2O \rightarrow CH_2O + NH_4^+ + CO_2 + 2H^+ + 2e^-$$

Marangoni and co-workers[33] reported that the solution after glycine electrolysis also contains methyl and trimethyl amines, which are probably formed by the interaction of formaldehyde and ammonium. Moreover, formaldehyde is possibly further oxidized at the anode to form formic acid.[47] Along with formaldehyde, formic acid is a possible source of carbon inclusion because carboxylic acids have been used as the carbon source for Fe-C alloy electrodeposition.[48, 49] Actually, formic acid has been employed as the source of carbon for the amorphous Fe-Cr-P-C alloy electrodeposition.[26, 50] Moreover, formic acid as well as formaldehyde is known to exhibit a brightening effect on Cr electroplating.[51] Formic acid is also known to form a very strong complex with trivalent Cr which significantly slows down Cr deposition,[19] which may explain the slight difference in the compositions of electrodeposits from the single-cell and the double-cell. The reported effects of formaldehyde as well as formic acid are analogous to our observations for the deposits obtained from the single-cell. Although detailed chemical analysis of the bath is necessary for precise identification of the reaction product(s) of glycine oxidation, we consider the carbon inclusion mechanism as follows (Fig. 11). In the single-cell, glycine is oxidized at the anode to form formaldehyde and/or formic acid. The oxidized products of glycine would subsequently diffuse and interact with the cathode, resulting in the incorporation of carbon in the FeCrNi deposit. Consequently, the deposit becomes supersaturated with carbon, stimulating the formation of the amorphous deposits. On the other hand, in the double-cell, the anodic glycine decomposition does not occur because the anode is separated from the cathode compartment. Therefore, the deposits from the double cell contain much less carbon, which allows for the formation of a crystalline alloy.

The formation of hexavalent chromium and ferric ions through oxidation of metal ions is also suggested by cyclic voltammetry. The existence of these ions is known to affect the electrodeposition. For example, hexavalent chromium ions in Cr electrodeposition baths are known to reduce the current efficiency because of the simultaneous reduction of hexavalent ions together with trivalent ions, while ferric ions are known to cause the inclusion of $Fe(OH)_3$, which precipitates at pH 2 to 3 even at a very low concentration due to its very low solubility product constant.[52] Although ferric ions are known to form a complex with glycine, such interaction of ferric ions with glycine is highly unlikely in a FeCrNi bath of pH 1. Therefore, the formation of ferric and hexavalent chromium ions by the anode oxidation are not considered to be responsible for the differences in the microstructure of between the deposits from the single- and double-cells, although more detailed studies are required for further discussion.

The effect of the anode reaction on the cathode process is of interest in order to obtain a further insight into the carbon inclusion mechanism. Therefore we also investigated the cathode reaction in the plating bath by cyclic voltammetry, as described in the supporting information (Figs. S1 and S2).
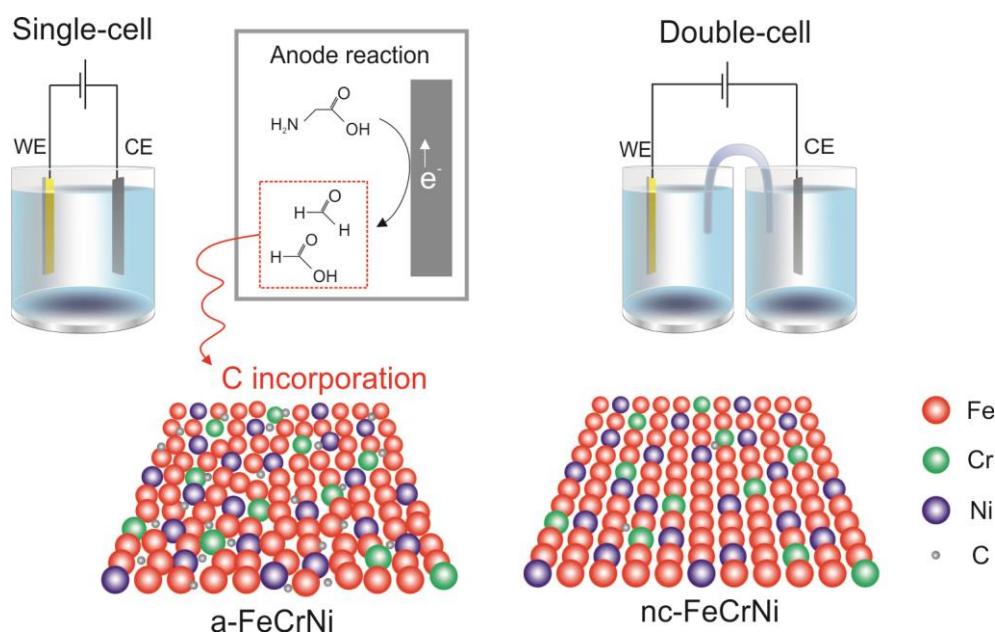

Fig. 11. Effects of the anodic oxidation of glycine on microstructure of FeCrNi electrodeposits.

However the detailed analysis of this electroplating system is difficult with this method due to hydrogen evolution as well as some reaction of a constituent of the base electrolyte which occurs in parallel with electrodeposition of FeCrNi.

In spite of the fact that there are still some issues to be solved, nc-FeCrNi electrodeposits showed an improved hardness compared to that of the a-FeCrNi, following the inverse Hall-Petch behavior, which is encouraging for the application of such alloy to the LIGA process.

Conclusions

We investigated the effects of anode reactions on the electrodeposition of FeCrNi alloy. Nanocrystalline FeNiCr (nc-FeCrNi) was obtained by employing a double-cell in which the anode electrode is separated from the cathode compartment, while, amorphous FeCrNi (a-FeCrNi) was electrodeposited in a conventional single-compartment cell. Crystallographic analysis by GI-XRD and TEM revealed that the as-deposited nc-FeCrNi consists of α-Fe grains with a size less than 10 nm, which are recrystallized to γ-Fe grains during heat treatment at 500°C. On the other hand, a-FeCrNi deposits recrystallize to α-Fe nc-FeCrNi upon annealing at 400°C, followed by further recrystallization to γ-Fe at 550°C. The chemical analysis of FeCrNi deposits as well as the electrochemical analysis revealed that the difference in crystal structure of these deposits is induced by carbon incorporation which is associated with the anodic oxidation product of glycine. The hardness of nc-FeCrNi was higher than that of a-FeCrNi, which corresponds to the inverse Hall-Petch relationship.

Acknowledgements

Notes and references

aEmpa - Swiss Federal Laboratories for Materials Science and Technology, Laboratory for Mechanics of Materials and Nanostructures, Feuerwerkerstrasse 39, 3602 Thun, Switzerland.

bEmpa - Swiss Federal Laboratories for Materials Science and Technology, Laboratory for Solid State Chemistry and Catalysis, Ueberlandstrasse 129, 8600 Dübendorf, Switzerland.

cEmpa - Swiss Federal Laboratories for Materials Science and Technology, Electron Microscopy Center, Ueberlandstrasse 129, 8600 Dübendorf, Switzerland.

dEleoss GmbH, Feuerwerkerstrasse 39, 3602 Thun, Switzerland.

eInstitute for Materials Science, University of Stuttgart, Heisenbergstrasse 3, DE-70569 Stuttgart, Germany.

1. J. R. Greer and J. T. M. De Hosson, *Progress in Materials Science*, 2011, **56**, 654-724.
2. N. Hansen, *Scripta Materialia*, 2004, **51**, 801-806.
3. C. C. Koch, *Mechanical Alloying*, 1992, **88**, 243-261.
4. R. Birringer, H. Gleiter, H. P. Klein and P. Marquardt, *Physics Letters A*, 1984, **102**, 365-369.
5. H. Gleiter, *Progress in Materials Science*, 1989, **33**, 223-315.
6. A. M. Elsherik and U. Erb, *Journal of Materials Science*, 1995, **30**, 5743-5749.
7. R. Gupta, K. Darling, R. K. Singh Raman, K. R. Ravi, C. Koch, B. S. Murty and R. O. Scattergood, *Journal of Materials Science*, 2012, **47**, 1562-1566.
8. A. R. Chezan, C. B. Craus, N. G. Chechenin, T. Vystavel, L. Niesen, J. T. M. De Hosson and D. O. Boerma, *Materials Science and Engineering: A*, 2004, **367**, 176-184.
9. X. Y. Wang and D. Y. Li, *Electrochimica Acta*, 2002, **47**, 3939-3947.
10. T. Roland, D. Retraint, K. Lu and J. Lu, *Scripta Materialia*, 2006, **54**, 1949-1954.
11. X. H. Chen, J. Lu, L. Lu and K. Lu, *Scripta Materialia*, 2005, **52**, 1039-1044.
12. H. W. Zhang, Z. K. Hei, G. Liu, J. Lu and K. Lu, *Acta Materialia*, 2003, **51**, 1871-1881.
13. T. Roland, D. Retraint, K. Lu and J. Lu, *Materials Science and Engineering: A*, 2007, **445–446**, 281-288.
14. G. Liu, J. Lu and K. Lu, *Materials Science and Engineering a-Structural Materials Properties Microstructure and Processing*, 2000, **286**, 91-95.
15. E. W. Becker, W. Ehrfeld, P. Hagmann, A. Maner and D. Munchmeyer, *Microelectronic Engineering*, 1986, **4**, 35-56.
16. C. U. Chisholm and R. J. G. Carnegie, *Electrodeposition and Surface Treatment*, 1973, **1**, 367-394.
17. H. Dahms and I. M. Croll, *Journal of the Electrochemical Society*, 1965, **112**, 771-775.
18. A. Baral and R. Engelken, *Journal of the Electrochemical Society*, 2005, **152**, C504-C512.
19. L. Philippe, C. Heiss and J. Michler, *Chemistry of Materials*, 2008, **20**, 3377-3384.
20. C. Niederberger, M. Gezat, M. Hasegawa and L. Philippe, in *Interfinish 2012 - The World Interfinish Congress of 2012*, Milano, Italy, Editon edn., 2012.
21. W. C. Oliver and G. M. Pharr, *Journal of Materials Research*, 1992, **7**, 1564-1583.
22. B. N. Lucas, W. C. Oliver, G. M. Pharr and J. L. Loubet, *MRS Online Proceedings Library*, 1996, **436**, null-null.
23. W. C. Oliver and G. M. Pharr, *Journal of Materials Research*, 2004, **19**, 3-20.
24. C. A. Snavely, *Transactions of the Electrochemical Society*, 1947, **92**, 537-577.
25. F. S. Yen, W. C. Chen, J. M. Yang and C. T. Hong, *Nano Letters*, 2002, **2**, 245-252.
26. J. C. Kang, S. B. Lalvani and C. A. Melendres, *Journal of Applied Electrochemistry*, 1995, **25**, 376-383.

27. X. Z. He, C. B. Xia, H. J. Wang, Z. Q. Gong and H. Y. Jiang, *Transactions of Nonferrous Metals Society of China*, 2001, **11**, 956-959.

28. M. Yasuda, H. Tsuji, Y. Ogata and F. Hine, *Journal of the Metal Finishing Society of Japan*, 1988, **39**, 282-284.

29. L. Sziraki, E. Kuzmann, M. El-Sharif, C. Chisholm, G. Principi, C. Tosello and A. Vertes, *Electrochemistry Communications*, 2000, **2**, 619-625.

30. A. G. Dolati, M. Ghorbani and A. Afshar, *Surface and Coatings Technology*, 2003, **166**, 105-110.

31. L. Xu, J. Du, S. Ge, N. He and S. Li, *Journal of Applied Electrochemistry*, 2009, **39**, 713-717.

32. G. Saravanan and S. Mohan, *International Journal of Electrochemical Science*, 2011, **6**, 1468-1478.

33. D. G. Marangoni, R. S. Smith and S. G. Roscoe, *Canadian Journal of Chemistry-Revue Canadienne De Chimie*, 1989, **67**, 921-926.

34. C. M. Welch, O. Nekrassova and R. G. Compton, *Talanta*, 2005, **65**, 74-80.

35. J. D. Giallonardo, U. Erb, K. T. Aust and G. Palumbo, *Philosophical Magazine*, 2011, **91**, 4594-4605.

36. A. M. Elsherik, U. Erb, G. Palumbo and K. T. Aust, *Scripta Metallurgica Et Materialia*, 1992, **27**, 1185-1188.

37. C. A. Schuh, T. G. Nieh and H. Iwasaki, *Acta Materialia*, 2003, **51**, 431-443.

38. Y. Zhou, U. Erb and K. T. Aust, *Philosophical Magazine*, 2007, **87**, 5749-5761.

39. J. T. Kim, S. H. Hong, C. H. Lee, J. M. Park, T. W. Kim, W. H. Lee, H. I. Yim and K. B. Kim, *Journal of Alloys and Compounds*, 2014, **587**, 415-419.

40. A. Slipenyuk and J. Eckert, *Scripta Materialia*, 2004, **50**, 39-44.

41. R. Bhowmick, R. Raghavan, K. Chattopadhyay and U. Ramamurty, *Acta Materialia*, 2006, **54**, 4221-4228.

42. J. Sort, J. Fornell, W. Li, S. Suriñach and M. D. Baró, *Journal of Materials Research*, 2009, **24**, 918-925.

43. F. Huerta, E. Morallon, F. Cases, A. Rodes, J. L. Vazquez and A. Aldaz, *Journal of Electroanalytical Chemistry*, 1997, **431**, 269-275.

44. F. Huerta, E. Morallon, F. Cases, A. Rodes, J. L. Vazquez and A. Aldaz, *Journal of Electroanalytical Chemistry*, 1997, **421**, 179-185.

45. D. G. Marangoni, I. G. N. Wylie and S. G. Roscoe, *Bioelectrochemistry and Bioenergetics*, 1991, **25**, 269-284.

46. Y. Takayama, *Bulletin of the Chemical Society of Japan*, 1933, **8**, 213-230.

47. Y. Takayama, T. Harada and S. Miduno, *Bulletin of the Chemical Society of Japan*, 1937, **12**, 342-349.

48. Y. Fujiwara, M. Izaki, H. Enomoto, T. Nagayama, E. Yamauchi and A. Nakae, *Journal of Applied Electrochemistry*, 1998, **28**, 855-862.

49. M. Izaki and T. Omi, *Metallurgical and Materials Transactions A*, 1996, **27**, 483-486.

50. J. C. Kang and S. B. Lalvani, *Journal of Applied Electrochemistry*, 1992, **22**, 787-794.

51. S. Hoshino, H. A. Laitinen and G. B. Hoflund, *Journal of the Electrochemical Society*, 1986, **133**, 681-685.

52. S. Gadad and T. M. Harris, *Journal of the Electrochemical Society*, 1998, **145**, 3699-3703.